Taylor & Francis
Taylor & Francis Group

Experimental inversion of optical diffraction tomography data with a nonlinear algorithm in the multiple scattering regime

Guillaume Maire[a], Jules Girard[a], Filip Drsek[a], Hugues Giovannini[a], Anne Talneau[b],
Kamal Belkebir[a], Patrick C. Chaumet[a]* and Anne Sentenac[a]

[a]*Institut Fresnel (UMR 6133), Université d'Aix-Marseille, Avenue Escadrille Normandie-Niemen, F-13397 Marseille
cedex 20, France;* [b]*CNRS, Laboratoire de Photonique et de Nanostructures, 91460 Marcoussis, France*

Optical diffraction tomography (ODT) is a recent imaging technique that combines the experimental methods of phase microscopy and synthetic aperture with the mathematical tools of inverse scattering theory. We present here in detail how this technique can be applied to highly scattering samples with a nonlinear inversion algorithm taking into account multiple scattering to reconstruct their permittivity profile. The obtained resolutions are substantially improved compared with wide-field microscopy and ODT performed with standard linear inversion procedures.

Keywords: optical diffraction tomography; nonlinear inversion algorithm

1. Introduction

The development of new optical imaging systems that can give the three-dimensional opto-geometrical parameters (shape, permittivity profile) of a sample at a sub-100 nm scale, while keeping a certain readiness of use, is presently a particularly active research topic [1–3]. Potential applications range across multiple fields in life and material science. In the nanofabrication domain, the manufacturing control of heterogeneous stacked platforms with typical length scales below 100 nm is, for instance, becoming increasingly important. In biology, the morphologic observation of the cell at such resolutions is also required to understand the different exchange mechanisms that are involved, as for example through the membrane of the cell. As standard optical microscopes perform only the measurement of the intensity of the light diffracted by the sample, they do not give a quantitative characterization of its permittivity profile [4]. Moreover, their diffraction limited resolution is incompatible with the investigation of samples presenting features smaller than 0.6λ, where λ is the illumination wavelength used. To circumvent these two difficulties, it has been proposed to measure the field in the near vicinity of the sample and reconstruct the permittivity map of the object by applying an inversion algorithm to the complex-valued data [5,1]. This promising approach is, however, experimentally challenging and the numerical reconstruction process is a difficult task.

Optical diffraction tomography (ODT) is a very attractive alternative to near-field microscopy. In this case, the diffracted field is measured with a far-field microscope and the image resolution is increased by illuminating the sample under various incident angles [6–11]. The permittivity map is obtained by using an inversion algorithm on the multiple recorded experimental dataset. This approach has received considerable interest in the last five years and various set-ups dedicated to both biological applications [8,7,11] and surface imaging [6,10,9] have been proposed. However, they all rely on a wave-object interaction model based on the single scattering approximation yielding fast and simple linear inversion algorithms. The drawback of this approach is that it is valid only for weakly scattering objects or specific geometries. In particular, it cannot be applied to samples presenting high or moderate permittivity contrasts, such as those encountered in the nanofabrication domain. This issue has been addressed theoretically and recently the necessity of using a non-linear inversion algorithm accounting for multiple scattering has been experimentally demonstrated [12]. In particular, it has been shown that this approach can provide a quantitative imaging of the permittivity map of highly scattering nanostructures with both an axial and transverse resolutions significantly improved compared with those of conventional microscopes.

In this paper, we present a comprehensive description of the whole procedure that can obtain

---
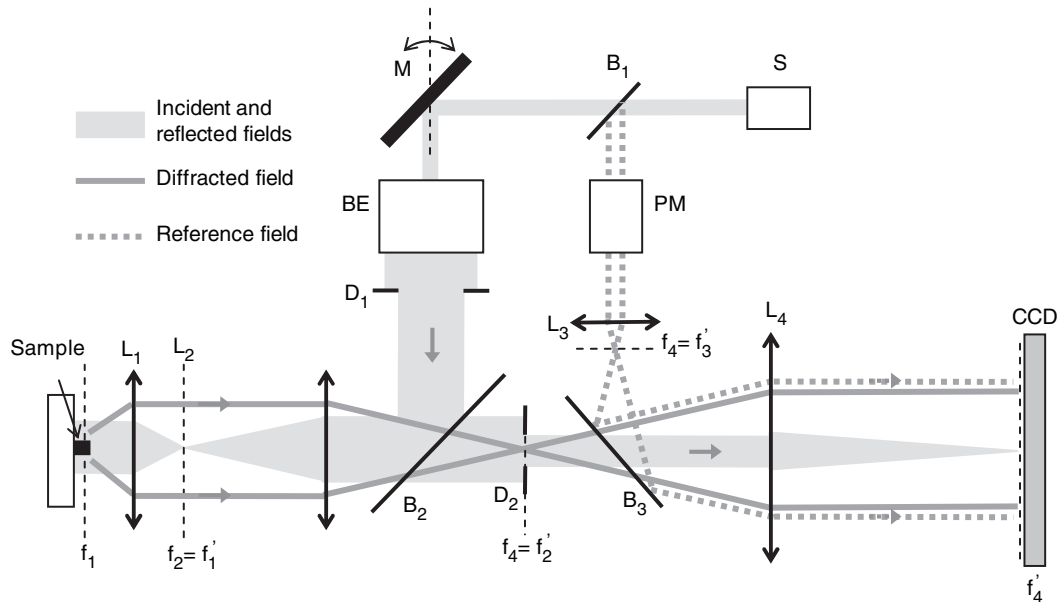
*Corresponding author. Email: patrick.chaumet@fresnel.fr

Figure 1. Sketch of the experimental set-up. L_1, L_2, L_3, L_4, lenses; f_i and f_i', associated object and image focal planes; S, laser source emitting at 633 nm; M, adjustable mirror; B_1, B_2, B_3, beam splitters; BE, beam expander; PM, phase modulator; D_1, D_2, diaphragms.

these results. In Section 2, the experimental set-up is described along with the measurement process and the normalization procedure applied to the data. In Section 3, the resolution approach used to solve the so-called 'forward scattering problem' is presented, and the inversion scheme used to retrieve the permittivity map of the sample from the data is exposed. Section 4 is devoted to the presentation of the experimental results obtained by following this procedure.

2. Experimental setup

2.1. Setup architecture

We have developed a synthetic aperture digital microscope working in reflection whose schematic is presented in Figure 1. The light emitted at 633 nm by a 10 mW Helium-Neon laser is divided into a reference beam, passing through an electro-optic phase modulator (PM), and a beam directed towards the sample. A rotating mirror permits us to vary this latter beam, while a beam expander (BE) and diaphragm D_1 generate a collimated beam with near homogeneous power density. The microscope objective (L_1) and the associated lens (L_2) enable us to illuminate the sample with a parallel beam over a wide range of incidence angles (typically ± 32 deg). The center of the mirror is conjugated, through the beam expander, L_2 and L_1, with the center of the sample. Thus, rotating the mirror varies the incidence angle without laterally shifting the illumination beam on the object.

The field diffracted by the object is collected by the microscope objective (Zeiss 'Fluar' $\times 20$, Numerical Aperture $= 0.75$ in air). An intermediary image of the object is obtained in the image focal plane of L_2, where a field diaphragm D_2 permits us to adjust the field of view without changing the diameter of the illumination beam. The diffracted field and the reference field are then superimposed coherently thanks to beam splitter B_3. The resulting beam is sent to a CCD camera via lens L_4 in order to make measurements in the far-field. The intermediary image is at the object focal plane of L_4, while the CCD camera is placed in the image focal plane and records a digital hologram, namely the interference pattern in the Fourier plane between the diffracted and reference fields. An additional lens L_5 can be placed after L_4 in order to observe the image of the sample. In this case, when the reference beam is shuttered, the system works as a conventional microscope illuminated by a coherent beam.

In the work presented here, the setup has been applied to samples consisting of resin rods with rectangular cross-sections, deposited on a silicon substrate (Figure 2). In all cases, the widths of the rods are much smaller than their lengths, and the incidence plane is perpendicular to the rods axis, while the incident electric field is parallel to it. This particular configuration allows the transformation of the three-dimensional vectorial electromagnetic problem into a two-dimensional scalar one.
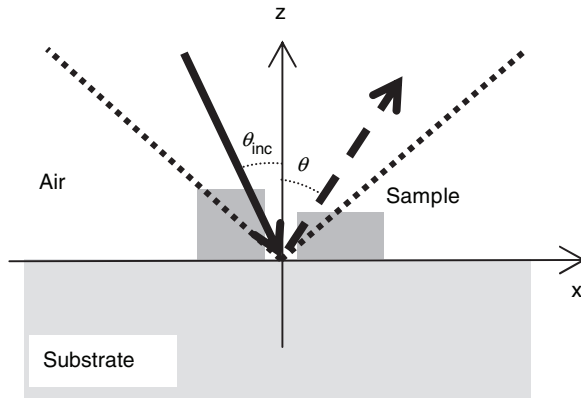
Figure 2. Schematic view of an ODT experiment in a reflection configuration. θ_{inc} is the angle of the incident illumination on the sample, θ is the angle indexing the diffraction directions. The dotted lines indicate the numerical aperture of the objective that collects the diffracted light.

2.2. Measurement procedure

At a first stage, the observation of the investigated sample in the image plane permits accurate placement of the sample at the focal plane of the objective. When this is done, the image of the sample and the image of the focus point F of the reference wave in the image focal plane of L_3 are obtained simultaneously on the CCD camera. Since the phase of the field diffracted by the sample is measured relative to the phase of the reference wave, F can be seen as the phase origin of the diffracted field. For the forward and the inverse scattering problems presented in Section 3, the diffracted field is calculated with a volumic integral approach over a finite spatial domain. For the 2D results presented here, this domain is a rectangle placed on the substrate. Choosing the location and the size of this investigation domain is similar to what is done in conventional microscopy when the microscope is focused on the sample. In ODT, the dimensions of the investigation domain are limited by the size of the matrices that can be treated by the computer. The calculation of the diffracted field assumes that the phase origin, called hereafter the modeling origin, is located on the substrate surface and in the center of the investigation domain. There is usually a mismatch between the modeling origin and the origin of the phase measured experimentally. This mismatch can lead to strong errors in the reconstruction of the permittivity map of the object. Therefore, before applying the inversion procedure to the measured field, it is necessary to shift numerically its phase so that the focus point F is conjugated to the modeling origin through lenses L_1 and L_2. Such a correction necessitates the knowledge of the mismatch distance that is evaluated through a procedure described

in Appendix 1. To minimize the transverse mismatch during the measurement, the sample is translated so that the image of F on the CCD camera is placed, as much as possible, at the center of the sample image.

To perform the measurement of the complex diffracted field, the CCD camera is placed in the Fourier plane and different illumination incidences are applied successively to the sample. The incidences are chosen so that a maximum portion of the Ewald sphere is covered by the resulting synthetic aperture. For a given illumination incidence, the amplitude and the phase of the field diffracted by the object are obtained by phase-shifting interferometry [13] from four digital holograms corresponding to four phase retardation $(0, \pi/2, \pi, 3\pi/2)$ introduced by the electro-optic modulator PM. In practice, a set of acquisitions (typically 100) are recorded and averaged for each phase retardation to increase the signal to noise ratio.

When the CCD camera records a digital hologram, it also detects the specular reflection of the incident beam on the sample substrate. This reflection is focused on the camera and produces far higher signal level than the diffracted field. Therefore, two measurements are performed for each incidence angle: one at low incident intensity (by attenuating the incident beam with an optical density) for measuring the reflected beam and the diffracted data in its vicinity, and one at high intensity for measuring the diffracted data further from the reflection. Merging the diffracted fields obtained for each intensity provides a good sensitivity over the whole camera, avoiding saturation at the reflection focus [8].

2.3. Data processing

In order to obtain a quantitative reconstruction of the optogeometrical parameters of the sample, a normalization procedure has to be applied to the experimental data before applying the inversion procedure to the diffracted fields obtained for the different illumination incidences.

2.3.1. Angular calibration

The inversion of experimental data necessitates a precise knowledge of the incidence angles and diffraction angles involved during the measurement. Each pixel of the CCD camera corresponds to one diffraction angle. The pixel related to diffraction along the normal incidence can be determined by simple geometrical considerations. As the microscope objective collects the light diffracted with angles up to around $46°$, that is well above Gauss conditions, a simple relation between pixel position and diffraction angle is, however, not necessarily straightforward to establish.

To determine this correspondence clearly, we therefore use a reference sample with known geometry and permittivity, illuminated along normal incidence. For the results presented in this paper, the reference sample is a resin rod of rectangular cross section, 100 nm high and 5 μm wide. The comparison of the experimental data with the diffracted field calculated with the simulation approach presented in Section 3 permits us to determine the relation between the pixel position and the diffraction angle. When characterizing an unknown object, this calibration is also used to determine the incidence angle of the illuminating wave thanks to the specular reflection on the sample substrate that is focused on a pixel of the CCD camera.

2.3.2. Restitution of the far-field phase profile

As our inversion algorithm reconstructs the sample permittivity map from far-field diffracted fields, our setup has been developed accordingly to perform such far-field measurements. However, the phase of the experimental data is corrupted by the lenses' aberrations and setup misalignment, which generate an additional unwanted phase distortion that has to be corrected. This distortion is also determined by using a reference sample, in practice the same as presented above. The experimental data are compared with the simulation ones for various illumination incidences. The discrepancy between the phase profiles is due to the unwanted phase distortion, but also to the fact that the phase origin is not exactly situated at the same location in the experimental and modelling configurations. Indeed, when the sample is illuminated with a plane wave of wavevector $\mathbf{k}_{inc}$ and the diffracted field is detected in far-field along the direction given by wavevector $\mathbf{k}$, the dependence of the diffracted phase on the position of the phase origin follows the relation:

$$\varphi_d(\mathbf{k}_{inc}, \mathbf{k}) = \varphi_0(\mathbf{k}_{inc}, \mathbf{k}) + (\mathbf{k} - \mathbf{k}_{inc}) \cdot \mathbf{d}, \qquad (1)$$

where $\mathbf{d}$ is the vector position shift of the phase origin relative to the modeling origin, φ_d and φ_0 the diffracted phase when the origin is taken at the position $\mathbf{d}$ and at the modeling origin, respectively. The mismatch $\mathbf{d}$ has therefore to be corrected before being able to extract the phase distortion due to aberrations. $\mathbf{d}$ cannot be evaluated by the procedure presented in Appendix 1 since it supposes that the aberrations have already been corrected. For the 2D reflection configuration we study here, Equation (1) can be rewritten as follows

$$\varphi_d(\mathbf{k}_{inc}, \mathbf{k}) = \varphi_0(\mathbf{k}_{inc}, \mathbf{k}) + k_0 d_x(\sin\theta - \sin\theta_{inc})$$
$$+ k_0 d_z(\cos\theta + \cos\theta_{inc}), \qquad (2)$$

where d_x and d_z are the projections of $\mathbf{d}$ onto the x-axis and the z-axis, respectively. φ_0 is assumed to be given by the theoretical calculations. To determine the two components d_x and d_z, φ_d is firstly plotted as a function of $\sin\theta$. For small angles, we can consider that no aberrations are involved and that $\cos\theta \approx 1$, so that φ_d is only sensitive to the phase shift variations due to d_x. It can be extracted by subtracting the theoretical profile φ_0 and calculating the slope of the remaining affine function. After the compensation of the phase shift due to d_x, φ_d is then plotted as a function of $\cos\theta$ for angles within the Gauss conditions, and the same process as before is applied to extract d_z. In practice, we observed that aberrations in the setup can be totally ignored for angles typically below 13 deg. Once the influence of both d_x and d_z has been corrected, the discrepancy between φ_0 and φ_d provides the phase distortion due to aberrations and setup misalignment.

2.3.3. Amplitude and phase normalization

The resolution improvement brought by the synthetic aperture is based on the merging of the diffracted data over the differently used incidences. This assumes that the scattered field is measured for each incidence under the same experimental conditions. Unfortunately, it is in practice hindered by several issues. The phase between the signal beam and the reference beam may change due to thermal and/or mechanical drifts or simply because the optical path of the incident beam is different when the incidence angle changes. Fluctuations of the laser source may also occur and change the amplitude of the illumination for different incidences. As a result, it is necessary to match the scattered fields both in amplitude and in phase.

Before explaining how this matching is performed, we first recall some general expressions of the field E_d scattered by a two-dimensional object when illuminated by a plane wave of amplitude A_{inc}. The plane wave expansion of the scattered field can be formulated as

$$E_d = A_{inc} \int \tilde{e}_d(\alpha) \exp(i\alpha x + i\gamma z) d\alpha, \qquad (3)$$

where $\tilde{e}_d$ denotes the complex amplitude of the plane wave component whose wavevector projections onto the x-axis and the z-axis are α and γ, respectively. In the far-field and along a given direction indexed by α, the scattered field E_d can be approximated as [14]:

$$E_d = A_{inc} \tilde{e}_d(\alpha)\gamma(\alpha)\sqrt{\frac{2\pi}{k_0 r}} \exp(ik_0 r \pm i\pi/4), \qquad (4)$$

where $k_0 = 2\pi/\lambda$ is the wavenumber in the vacuum and r the propagation distance from the object. Keeping a

2D description for the signal detected in our setup, the Poynting vector flux $\delta\sigma_d$ of E_d across a pixel placed at the distance r can be expressed as

$$\delta\sigma_d \propto A_{\mathrm{inc}}^2 |\tilde{e}_d(\alpha)\gamma(\alpha)|^2 \frac{2\pi}{k_0} \delta\theta, \qquad (5)$$

with $\delta\theta$ the angular span covered by the pixel. The inversion algorithm we use to reconstruct the sample necessitates as input data the products $\tilde{e}_d(\alpha)\gamma(\alpha)$ for a set of diffraction angles and incidence angles. The matching procedure must therefore also normalize the experimental data to obtain this input format.

The matching of the different scattered fields is based on a normalization ensuring that each specularly reflected field is equal to the theoretical reflectivity of the substrate. This implies that the permittivity of the substrate is known and that the amplitude of the diffracted field is negligible as compared with that of the specular beam. This assumption is verified even for strong scattering samples if the overall size of the scattering object is small compared to that of the field of view.

The phase matching is performed by imposing at the specular focus for each incidence a phase equal to the argument of the amplitude reflectivity of the substrate. If **d** is the vector shift of the phase origin, the reflectivity can be written for a given incidence as:

$$r_{\mathrm{inc}} = \rho_{\mathrm{inc}} \exp(i\phi_{\mathrm{inc}} + i(\mathbf{k}_r - \mathbf{k}_{\mathrm{inc}}) \cdot \mathbf{d}), \qquad (6)$$

where ρ_{inc} is the modulus of the reflectivity, ϕ_{inc} its argument when the phase origin is placed on the substrate, and $\mathbf{k}_r$ the wavevector of the specular reflection. It is therefore necessary to correct the phase origin mismatch thanks to the procedure described in Appendix 1 before normalizing the phases to the values taken by ϕ_{inc}.

To perform the amplitude matching, the specular field E_s can be described the same way as E_d with Equations (3) and (4), since it is transmitted by the diaphragm D_2 and focused on the CDD camera by the lens L_4. The Poynting vector flux $\delta\sigma_s$ of E_s is derived from Equation (5):

$$\delta\sigma_s \propto \rho_{\mathrm{inc}}^2 A_{\mathrm{inc}}^2 |\tilde{e}_s(\alpha)\gamma(\alpha)|^2 \frac{2\pi}{k_0} \delta\theta, \qquad (7)$$

where $\tilde{e}_s$ is the equivalent of $\tilde{e}_d$ but for the field E_s. It can be calculated analytically by solving the Fraunhofer diffraction for a slit of width $2a$, with a the radius of diaphragm D_2:

$$\tilde{e}_s(\alpha) = \frac{a}{\pi} \mathrm{sinc}[a(\alpha_{\mathrm{inc}} - \alpha)], \qquad (8)$$

where α_{inc} is the projection onto the x-axis of the wavevector of the incident plane wave. Therefore, Equations (7) and (8) permit evaluation of the Poynting vector flux at the reflection focus and extraction of the normalization factor $A_{\mathrm{inc}}^2 \frac{2\pi}{k_0} \delta\theta$. The experimental data are divided by this factor to obtain the amplitude matched product $|\tilde{e}_d(\alpha)\gamma(\alpha)|$ for each incidence.

Such a normalization supposes that the radius a is known. To evaluate it, we perform a 2D inverse Fourier transform of the field diffracted by the sample on the whole CCD camera for a given incidence. It provides the field at the object focal plane of lens L_4 and therefore an image of diaphragm D_2 from which the radius a can be evaluated. Note that the obtained value has to be divided by the magnification between the focal planes f_1 and f_2' so that the same angular scale can be applied to both the sample and the diaphragm diffracted data.

To conclude this section on data processing, we have developed a normalization procedure that permits us to correct the unwanted phase distortion due to aberrations and setup misalignment as well as the phase origin mismatch. The calibration is also used to perform the amplitude and phase matching of the diffracted fields, and convert the experimental data to an adequate input for the inversion algorithm. We have checked on various samples that, thanks to this procedure, the measured diffracted far-field was close to that obtained with rigorous simulations. As an example, Figure 3 presents the results obtained for a sample made of three resin rods of rectangular cross sections when illuminated with an incidence angle of $5.3°$. Their height is 110 nm, their width 220 nm and they are separated side by side by 300 nm. Figure 3(a) shows, as a function of the diffraction angle, the simulated diffracted phase (blue curve), the experimental diffracted phase before normalization (red curve) and the phase shift due to aberrations (black curve) obtained on the reference sample. Note that for the experimental phase, the phase shift due to the phase origin mismatch has already been corrected. In Figure 3(b), the normalization procedure has been applied to the experimental phase. Figure 3(c) presents the logarithm of the simulated diffracted amplitude (blue curve) and of the experimental one after normalization (red curve).

3. Reconstruction of the sample permittivity map

3.1. Formulation of the forward scattering problem

Throughout the paper, a time dependence on $\exp(-i\omega t)$ is assumed and ignored. The y component
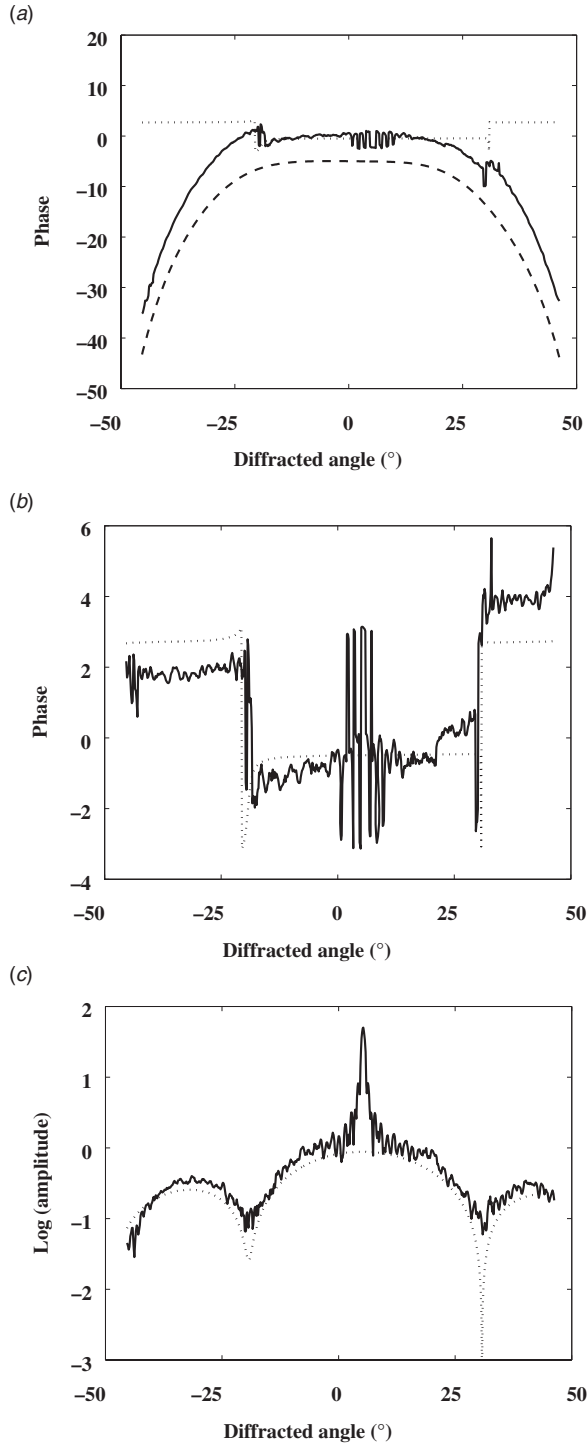
(a)

(b)

(c)

Figure 3. Field diffracted by a three rod sample when illuminated at 5.3°. (a) Simulated diffracted phase (dotted line), experimental diffracted phase before normalization (solid line), and phase shift due to aberrations (dashed line, shifted downwards for clarity) as a function of diffraction angle [°]. (b) Simulated diffracted phase (dotted line) and experimental diffracted phase after normalization (solid line) as a function of diffraction angle. (c) Logarithm of the simulated diffracted amplitude (dotted line) and of the experimental diffracted amplitude after normalization (solid line) as a function of diffraction angle.

of the electric field $E_l(x, z)$ at the point (x, z) satisfies the Helmholtz equation

$$\Delta E_l(x, z) + \varepsilon_b(z)k_0^2 E_l(x, z) = S_l - k_0^2 \chi(x, z) E_l(x, z),$$

(9)

where $k_0 = 2\pi/\lambda$ is the wave number in vacuum, S_l is the source that radiates the incident beam and $\varepsilon_b(z)$ is the permittivity of the background medium. The subscript l in E_l indicates the dependence of the electric field on the incident field generated by S_l. Introducing the Green function solution of

$$\Delta G(x, z; x', z') + \varepsilon_b(z)k_0^2 G(x, z; x', z') = -\delta(x - x'; z - z')$$

(10)

that satisfies the outgoing-wave boundary condition, one can rewrite the differential Equation (9) as an integral equation

$$E_l(x, z) = E_l^{\mathrm{ref}}(x, z) + k_0^2 \int G(x - x'; z, z') \chi(x', z')$$
$$\times E_l(x', z')\mathrm{d}x'\mathrm{d}z',$$

(11)

where E_l^{ref} is the field that would exist without the presence of objects, $G(x - x'; z, z')$ denotes the field at (x, z) radiated by a line source placed at (x', z') above the substrate and $\chi(x', z') = \varepsilon(x', z') - \varepsilon_b(z')$ is the permittivity contrast, which is nonzero only inside objects. Equation (11) can be used in the far-field zone to describe the scattered field measured in the Fourier plane and in the near-field zone to estimate the field inside the objects.

For the sake of simplicity, we rewrite Equation (11) for near-field (electromagnetic field inside the scattering objects) and for the far-field (observed scattered far-field) using operator notation:

$$E^{\mathrm{d}} = \mathbf{K}\chi E_l,$$

(12)

$$E_l = E_l^{\mathrm{ref}} + \mathbf{G}\chi E_l.$$

(13)

The forward problem can be solved in two steps. One can deduce from Equation (13) the total field inside the scattering objects and substituting the value of this field in Equation (12) leads to the scattered far-field.

3.2. Inversion procedure

The inverse scattering problem now consists of finding the contrast χ in the investigating domain Ω so that the diffracted field associated with χ matches the measured one f_l. We suggest here to solve this ill-posed and nonlinear problem iteratively [14,15]. The general principle of this technique is to build up two sequences related to contrast and total field inside the

investigating domain $\{\chi_n\}$ and $\{E_{l,n}\}$, respectively, according to the following recursive relations:

$$E_{l,n} = E_{l,n-1} + \alpha_{l,n;v}v_{l,n} + \alpha_{l,n;w}w_{l,n}, \quad (14)$$

$$\chi_n = \chi_{n-1} + \beta_n d_n, \quad (15)$$

where $v_{l,n}$, $w_{l,n}$ and d_n are search directions with respect to the total field E_l and to the contrast. The choice of these directions will be discussed later on in the paper. The scalar coefficients α and β are weights that are chosen at each iteration step n so as to minimize the normalized cost functional $\mathcal{F}_n(\chi_n, E_{l,n})$ given by

$$\mathcal{F}_n(\chi_n, E_{l,n}) = W_\Omega \sum_{l=1}^{L} \|h_{l,n}^{(1)}\|_\Omega^2 + W_\Gamma \sum_{l=1}^{L} \|h_{l,n}^{(2)}\|_\Gamma^2, \quad (16)$$

where the normalizing coefficients W_Ω and W_Γ are as follows:

$$W_\Omega = \frac{1}{\sum_{l=1}^{L} \|E_l^{\text{ref}}\|_\Omega^2}, \quad W_\Gamma = \frac{1}{\sum_{l=1}^{L} \|f_l\|_\Gamma^2}. \quad (17)$$

The subscripts Γ and Ω are included in the norm $\|\cdot\|$ and later in the inner product $\langle\cdot,\cdot\rangle$ to indicate the domain of integration. Functions $h^{(1)}$ and $h^{(2)}$ are two residual errors computed from Equations (13) and (12), respectively.

$$h_{l,n}^{(1)} = E_l^{\text{ref}} - E_{l,n} + \mathbf{G}\chi_n E_{l,n}, \quad (18)$$

$$h_{l,n}^{(2)} = f_l - \mathbf{K}\chi_n E_{l,n}. \quad (19)$$

The use of a priori information may improve the inversion algorithm. In the present work, we incorporated the information stating that the objects under test are dielectric with no losses [14,15]. Instead of retrieving a complex function χ_n, only one real valued auxiliary function ξ_n is reconstructed such that

$$\chi_n = \xi_n^2. \quad (20)$$

Once the updating directions d_n, $v_{l,n}$ and $w_{l,n}$ are chosen, $\mathcal{F}_n$ is a nonlinear expression with $2L$ complex variables $(\alpha_{l;v}, \alpha_{l;w})$ and one real variable β_n. The minimization of $\mathcal{F}_n$ is accomplished using the Polak-Ribière conjugate gradient method.

As as updating direction d_n, we take the standard Polak-Ribière conjugate gradient direction

$$d_n = g_n + \gamma_n d_{n-1}, \quad (21)$$

with

$$\gamma_n = \frac{\langle g_n, g_n - g_{n-1}\rangle}{\|g_{n-1}\|_\Omega^2}, \quad (22)$$

where g_n is the gradient of the cost functional $\mathcal{F}(\xi, E_l)$ with respect to ξ evaluated at the $(n-1)$th step assuming that the total field does not change. This gradient is given by

$$g_n = 2\xi_{n-1}\Re e\left[W_\Omega \sum_{l=1}^{L} \bar{E}_{l,n-1}\mathbf{G}^\dagger h_{l,n-1}^{(1)} - W_\Gamma \sum_{l=1}^{L} \bar{E}_{l,n-1}\mathbf{K}^\dagger h_{l,n-1}^{(2)} \right], \quad (23)$$

where the overbar denotes the complex conjugate. The operators $\mathbf{G}^\dagger$ and $\mathbf{K}^\dagger$ are the adjoint operators of $\mathbf{G}$ and $\mathbf{K}$, respectively.

The search direction $v_{l,n}$ is of the same type as the one chosen for the object function ξ_n

$$v_{l,n} = g_{l,n;E} + \gamma_{l,n;E}v_{l,n-1} \quad (24)$$

with

$$\gamma_{l,n;E} = \frac{\langle g_{l,n;E}, g_{l,n;E} - g_{l,n-1;E}\rangle_\Omega}{\|g_{l,n-1;E}\|_\Omega^2}, \quad (25)$$

where $g_{l,n;E}$ is the gradient of the cost functional $\mathcal{F}_n(\xi, E_l)$ with respect to the total field E_l evaluated at the $(n-1)$th step, assuming that ξ does not change.

$$g_{l,n;E} = W_\Omega\left[\bar{\chi}_{n-1}\mathbf{G}^\dagger h_{l,n-1}^{(1)} - h_{l,n-1}^{(1)}\right] - W_\Gamma\bar{\chi}_{n-1}\mathbf{K}^\dagger h_{l,n-1}^{(2)}. \quad (26)$$

The second updating direction $w_{l,n}$ for the total field is given by

$$w_{l,n} = \tilde{E}_{l,n-1} - E_{l,n-1}, \quad (27)$$

where $\tilde{E}_{l,n-1}$ is the total field, computed from Equation (13), that would be present in the investigating domain Ω if the contrast χ is estimated by ξ_{n-1}^2.

$$\tilde{E}_{l,n-1} = \left[\mathbf{1} - \mathbf{G}\xi_{n-1}^2\right]^{-1}E_l^{\text{ref}}. \quad (28)$$

Notice that the nonlinear inversion algorithm presented in this section will be restricted to a bounded investigating domain above the substrate (i.e. $\varepsilon_b = 1$) it means that we know that the objects are above the substrate.

4. Experimental results

We illustrate here the performances of our nonlinear inversion algorithm on data obtained with the ODT set-up presented in Section 2. As mentioned in that section, the setup has been calibrated on a reference sample that is a rectangular resin rod of width 5 μm and height 100 nm to quantify both the diffraction angles and the phase distortion induced by aberrations.

The measurements presented hereafter have been carried out on the three rod sample used at the end of Section 2 to illustrate the data normalization procedure. The rods are deposited on a silicon substrate, and the relative permittivities of silicon and of the resin are $15.07 + 0.148i$ and 2.66, respectively. The diffracted fields have been measured for a set of 668 observation angles ranging from -46 to $+46$ degrees. This was performed for 10 incidence angles between -32 and 32 degrees.

Figure 4 presents the results of the nonlinear inversion compared with other characterization techniques. Figure 4 shows the height profile given by an atomic force microscope (AFM) and provides an accurate reference measurement for the sample dimensions. Figure 4(b) presents firstly the intensity profile obtained with a wide-field optical microscope that operates with red incoherent illumination and with an objective (Zeiss 'Epiplan' ×100) whose numerical aperture is the same as in our ODT setup (solid line). It also gives the squared modulus of the sample

reflectance (dotted line) obtained by applying to the data a linear inversion algorithm (detailed below). Figure 4(c) is the map of relative permittivity of the sample given by the nonlinear inversion, and the white line indicates the actual sample dimensions. In Figure 4(d), the permittivity profile along the white dashed line of Figure 4(c) is plotted for the nonlinear case (blue dashed curve) and compared to the actual profile (black curve) and the one obtained with the back-propagation procedure (red dotted curve).

The three rods are separated by a center-to-center distance of 500 nm that corresponds to the Abbe limit for the numerical aperture (NA), the incidence angles and the wavelength used here. As a result, the rods can hardly be distinguished with wide-field microscopy on Figure 4(b). The resolution is, however, not improved when the ODT setup is combined to a simple linear inversion algorithm (ODT-LIA, dotted profile on Figure 4(b)) used in most surface imaging [6]. Once the digital holograms have been recorded in the Fourier plane for all incidences, this algorithm consists
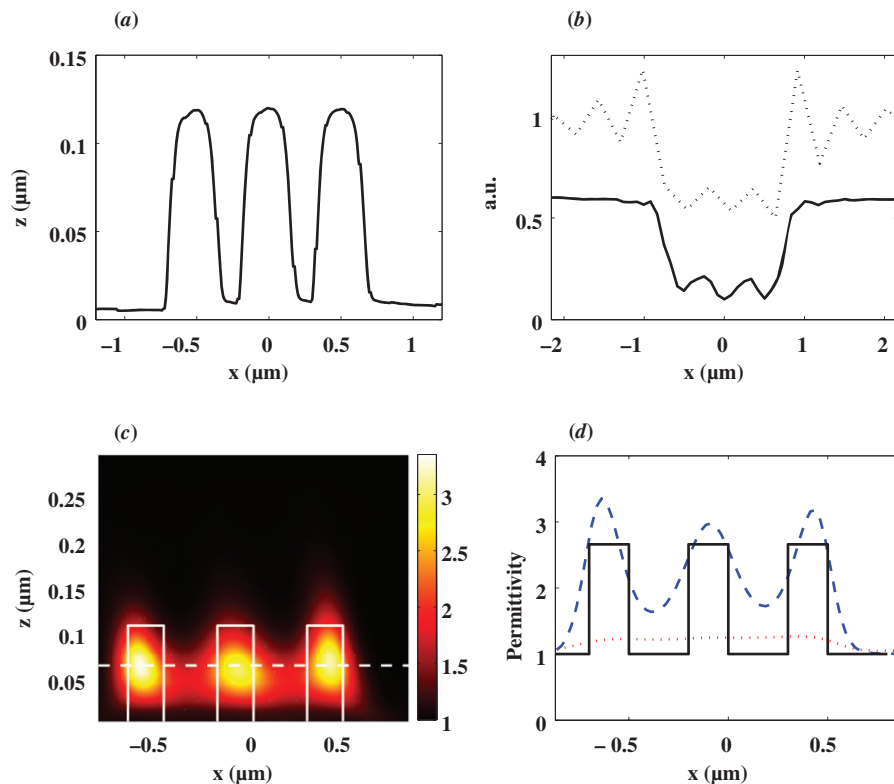

Figure 4. The sample is constituted of three rectangular rods of resin deposited on a silicon substrate. The rods' height and width are 110 nm and 200 nm, respectively. The rods are separated by 300 nm side to side. (a) Height profile provided by the AFM. (b) Dotted line: squared modulus of the reflectance obtained with ODT-LIA approach. Solid line: Intensity measured at the image plane of a wide-field optical microscope with NA = 0.75 and red incoherent light. (c) Map of the permittivity obtained with the non-linear inversion algorithm applied to the same data as that used in the ODT-LIA approach. (d) Comparison along the white dashed line plotted in (c) of the reconstructed permittivity (blue dashed line) with the actual value (black solid line) and the one provided by back-propagation (red dotted line). (The color version of this figure is included in the online version of the journal.)

of joining all the holograms into a global set of data and performing a 2D inverse Fourier transform. Since our samples are invariant along one transverse direction, the inverse Fourier transform is restricted here to one dimension. This linear inversion procedure relies on an approximate modelization of the field existing at the object focal plane of the microscope, that is,

$$E(\boldsymbol{x}) = R(\boldsymbol{x})E_{\text{inc}}(\boldsymbol{x}) \qquad (29)$$

where R is the reflectance of the structured sample, and E_{inc} is the incident field. Under this approximation, the hologram obtained in the Fourier plane at the reciprocal variable α is proportional to $\tilde{R}(\alpha - \alpha_{\text{inc}})$ where $\tilde{R}$ is the Fourier transform of R and α_{inc} is the transverse wavevector of the incident plane wave. This approach can be derived from our formulation of the forward scattering problem if single scattering and paraxial approximation are assumed in Equation (12). The disappointing performances of such an approach, as compared to those of the wide-field microscope, stem mainly from the Gibbs phenomenon and the strong sensitivity to the data noise that deteriorate the reconstructed reflectance. On the other hand, performing ODT with our non-linear inversion algorithm (ODT-NLIA) gives a permittivity map where the three rods are perfectly separated (Figures 4(c) and (d)). The benefit of the iterative algorithm appears clearly on Figure 4(d) where the permittivity profile given by the final iteration (blue dashed line) is compared with the one initially provided by the back-propagation procedure (red dotted line) that fails to separate the rods. In our opinion, the significant improvement brought by the ODT-NLIA over the ODT-LIA is essentially due to the fact that: first, it takes advantage of the a priori information that the objects are deposited on a known substrate and that their permittivity is positive; second, it is based on a rigorous calculation of the diffracted field so that it is not plagued by any model error and it has potential access to spatial frequencies that are higher than that given by the single-scattering analysis. Note that this ODT-NLIA setup has been recently used to resolve rods beyond the Abbe limit [12].

5. Conclusion

We present here in detail an optical diffraction tomography setup and the corresponding data normalization procedure so that a nonlinear inversion algorithm can be applied to reconstruct the permittivity map of highly scattering samples from their diffracted fields. This approach enables us to compute rigorously the diffraction process by taking into account multiple scattering, contrarily to linear inversion algorithms that are mainly restricted to cases where the Born approximation is valid. It is shown here that using a linear approach for high permittivity contrast samples does not increase the imaging performances compared with conventional wide-field microscopy, whereas the nonlinear iterative inversion both improves the resolution and correctly estimates the sample permittivity. We believe such an approach is a promising path for high resolution quantitative imaging of complex objects. The quantitative information provided by this kind of imager (permittivity distribution with high axial and transverse resolutions), is, to our knowledge, out of reach of all present imaging systems. It is interesting to note that a priori information can be inserted in the iterative algorithm to further improve the inversion. Sub-100 nm resolution in both axial and transverse directions is expected with the latest objectives presenting a numerical aperture about 1.5.

References

[1] Carney, P.S.; Frazin, R.A.; Bozhevolnyi, S.; Volkov, V.S.; Boltasseva, A.; Schotland, J.C. *Phys. Rev. Lett.* **2004,** *92,* 163903.

[2] Sentenac, A.; Chaumet, P.C.; Belkebir, K. *Phys. Rev. Lett.* **2006,** *97,* 243901.

[3] Liu, Z.; Lee, H.; Xiong, L.; Sun, C.; Zhang, X. *Science* **2007,** *315,* 1686.

[4] Streibl, N. *J. Opt. Soc. Am. A* **1985,** *2,* 121–127.

[5] Panasyuk, G.Y.; Markel, V.A.; Carney, P.S.; Schotland, J.C. *Appl. Phys. Lett.* **2006,** *89,* 22111.

[6] Alexandrov, S.A.; Hillman, T.R.; Gutzler, T.; Sampson, D.D. *Phys. Rev. Lett.* **2006,** *97,* 168102.

[7] Choi, W.; Fang-Yen, C.; Badizadegan, K.; Oh, S.; Lue, N.; Dasari, R.; Feld, M.S. *Nat. Methods* **2007,** *4,* 717–719.

[8] Lauer, V. *J. Microsc.* **2002,** *205,* 165–176.

[9] Neumann, A.; Kuznetsova, Y.; Brueck, S.R. *Opt. Express* **2008,** *16,* 6785–6793.

[10] Mico, V.; Zalevsky, Z.; Garcia-Martinez, P.; Garcia, J. *J. Opt. Soc. Am. A* **2006,** *23,* 3162–3170.

[11] Debailleul, M.; Simon, B.; Georges, V.; Haeberlé, O.; Lauer, V. *Meas. Sci. Technol.* **2008,** *19,* 074009.

[12] Maire, G.; Drsek, F.; Girard, J.; Giovannini, H.; Talneau, A.; Konan, D.; Belkebir, K.; Chaumet, P.C.; Sentenac, A. *Phys. Rev. Lett.* **2009,** *102,* 213905.

[13] Yamaguchi, I.; Zhang, T. *Opt. Lett.* **1997,** *22,* 1268–1270.

[14] Belkebir, K.; Sentenac, A. *J. Opt. Soc. Am. A* **2003,** *20,* 1223–1229.

[15] Belkebir, K.; Tijhuis, A.G. *Inverse Probl.* **2001,** *17,* 1671–1688.

[16] Belkebir, K.; Kleinman, R.E.; Pichot, C. *IEEE T. Microw. Theory* **1997,** *45,* 469–476.

[17] Belkebir, K.; Chaumet, P.C.; Sentenac, A. *J. Opt. Soc. Am. A* **2005,** *22,* 1889–1897.

Appendix 1. Estimation of the phase origin mismatch

In this appendix we present a method that provides a correction of the origin of the phase of data. In fact, our first inversion results were deceiving and we found out that the problem was that the origin of the phase in the experimental device is different from the one that is used in the scattering model of the inversion.

Let f_l be the measurement and $\mathbf{u} = u_x \hat{x} + u_z \hat{z}$ the two-dimensional vector representing the distance between the experimental phase origin and the 'theoretical' one. As a consequence, bearing in mind that the sample is illuminated by a plane wave and the measurements are carried out in the far-field zone, the distortion of the phase is given by

$$\tilde{f}_l = f_l \exp(i[\mathbf{k} - \mathbf{k}_{\mathrm{inc}}] \cdot \mathbf{u}). \tag{30}$$

The problem is now stated as finding the two-dimensional vector $\mathbf{u}$ so that the associated scattered field $\tilde{f}_l$ provides a best initial guess for the inversion scheme thanks to the backpropagation procedure [16,17]. This is accomplished by minimizing the following cost function $\mathcal{G}$

$$\mathcal{G} = \sum_{l=1}^{L} \left\| \tilde{f}_l - \gamma \mathbf{K}\mathbf{K}^\dagger \tilde{f}_l \right\|_\Gamma \tag{31}$$

where γ is a scalar. Note that, $\mathbf{K}^\dagger \tilde{f}_l$ is the induced current within Ω computed in the backpropagation technique. The minimization of the cost function $\mathcal{G}$ which depends on parameters u_x, u_z and γ is carried out thanks to the simplex method. Once the two-dimensional vector $\mathbf{u}$ is determined, the corrected scattered field $\tilde{f}_l$ is computed and used as input data from the inversion.